RSC Applied Interfaces

ROYAL SOCIETY OF CHEMISTRY

PAPER

View Article Online
View Journal

Cite this: DOI: 10.1039/d5lf00343a

Interfacial, solvent-free room-temperature adsorption of quinone derivatives on activated carbon for sustainable energy storage electrodes

Hiroyuki Itoi, *[a] Ryoma Ito,[a] Manato Matsuo,[a] Yusuke Higashi,[a] Hayato Suzuki,[a] Ginga Saeki,[a] Takafumi Ishii [b] and Yoshimi Ohzawa[a]

Redox-active quinone derivatives (QDs) were hybridized with activated carbon (AC) through a solvent-free, room-temperature process that requires only mixing the two components in a sealed container. Four representative QDs—tetramethyl-1,4-benzoquinone (TMBQ), 2,6-di-*tert*-butyl-1,4-benzoquinone (DBBQ), phenylbenzoquinone (PBQ), and naphthoquinone (NQ)—were examined. TMBQ, DBBQ, and NQ were rapidly adsorbed *via* interfacial interactions from the AC particle surfaces into the pores, whereas PBQ exhibited relatively slower adsorption. Importantly, water molecules inherently present in AC pores did not hinder QD adsorption, demonstrating that drying is unnecessary. By quantifying the water content in AC, adsorption levels could be precisely controlled without the need for heating or vacuum treatment. Structural and calorimetric analyses confirmed that adsorption was driven by strong π–π interactions. When evaluated in an aqueous H_2SO_4 electrolyte, the AC/QD hybrids showed extensive interfacial contact between QDs and conductive carbon surfaces, facilitating rapid and reversible redox reactions confined within the AC pores. As a result, the hybrids delivered significantly enhanced volumetric capacitances compared with pristine AC and maintained higher absolute volumetric capacitance even after 10 000 cycles, when employed as electrochemical capacitor electrodes. This interfacial adsorption strategy eliminates the need for organic solvents, heating, vacuum treatment, filtration, drying, purification, and specialized apparatus, underscoring the decisive role of interfaces in governing electrochemical behaviour. The findings demonstrate a sustainable and energy-efficient pathway to high-performance carbon–quinone hybrid electrodes, advancing interfacial science in electrochemical energy storage.

Received 5th November 2025,
Accepted 24th March 2026

DOI: 10.1039/d5lf00343a

rsc.li/RSCApplInter

1. Introduction

Liquid-phase adsorption is extensively employed to adsorb adsorbates onto porous materials. In industrial applications, this method is crucial for the removal of organic contaminants and impurities from water and food during purification processes.[1] Simultaneously, guest compounds are hybridized within the pores of porous materials in the liquid phase, synthesizing promising host/guest hybrids for electrical energy storage and electronics.[2–4] Organic solvents, chosen for their ability to dissolve organic compounds effectively, are frequently used in adsorption processes.[5,6] The resulting hybrids are then isolated through filtration and subsequent drying.[7,8] However, liquid-phase adsorption complicates the precise control of adsorption amounts, as not all adsorbates in the liquid phase can be fully adsorbed onto porous materials.[9–12] This inefficiency leads to solvent and adsorbate waste. Therefore, achieving accurate adsorption levels and minimizing waste are crucial.

Compared to liquid-phase adsorption, gas-phase adsorption involves heating a system containing both an adsorbate and an adsorbent, a process that vaporizes the adsorbate and accelerates adsorption.[13,14] As long as the adsorbate amount remains below the adsorbent's saturation capacity, gas-phase adsorption facilitates complete adsorption of the adsorbate, thus enabling accurate control of the adsorption amount. This precision is particularly beneficial for applications requiring consistent results, such as in electrode materials and electronic devices. Moreover, gas-phase adsorption does not require solvents or a drying process, making it an environmentally friendly method that reduces waste, streamlines manufacturing, and shortens optimization times.

We have developed a gas-phase adsorption method that allows for the hybridization of redox-active organic[15–21] and organometallic[22–24] compounds within the pores of porous carbons, facilitating the preparation of electrochemical

[a] *Department of Applied Chemistry, Aichi Institute of Technology, Yachigusa 1247, Yakusa-cho, Toyota, 470-0392, Japan. E-mail: itoi-hiroyuki@aitech.ac.jp*
[b] *Graduate School of Science and Technology, Gunma University, Kiryu, Gunma, 376-8515, Japan*

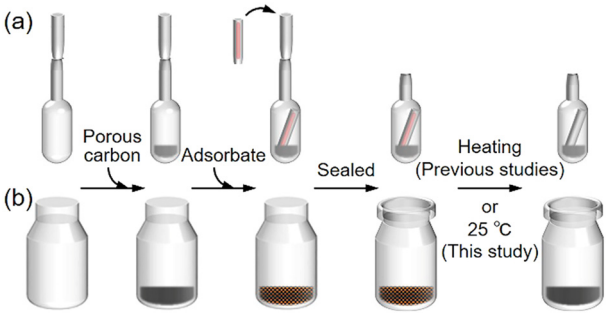

Scheme 1 Gas-phase adsorption: (a) direct method and (b) indirect method.

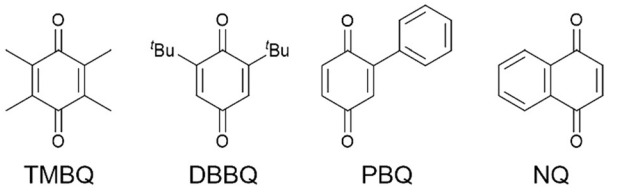

Fig. 1 Molecular structures of the redox-active quinone derivatives (QDs) used in this study.

capacitor electrodes without material waste. This hybridization results in an exceptionally large contact area between the hybridized materials and the highly conductive carbon surface, enabling a substantial charge transfer at the interface. Consequently, this facilitates rapid redox reactions, essential for achieving high power densities. Additionally, the hybridized redox-active materials contribute to a significant increase in volumetric capacitance, as this hybridization prevents the expansion of porous carbon particles upon adsorption. Furthermore, akin to the fixed battery sizes in electronic devices and smartphones, prioritizing volumetric over gravimetric capacitance is essential. This is due to the stringent volume constraints within these devices, making volumetric efficiency paramount in practical applications.[25] In the initial indirect method (Scheme 1a), a porous carbon sample was placed in a glass ampoule and dried by evacuation and heating; its dry mass was obtained by subtracting the mass of an empty ampoule from that of the ampoule containing the dried carbon. A measured amount of adsorbate was loaded into a capillary, the capillary was inserted into the ampoule, and the ampoule was sealed under vacuum. The sealed ampoule was then heated to the adsorbate's sublimation temperature to promote adsorption.[15,17] In the subsequent indirect method (Scheme 1b), the pre-dried porous carbon was placed in a vial, and its dry mass was determined from the increase in the vial's weight. The required amount of adsorbate was then added directly into the vial, which was sealed and mixed before heating. Unlike the indirect method, the direct method does not require evacuation prior to heating, and adsorption was found to occur at a lower temperature.[19,20] Despite the differences in preparation, the hybrids produced by both methods exhibited similar performance in electrochemical capacitors, with the direct method being significantly simpler than the indirect one.

In this study, we employed a room-temperature gas-phase adsorption approach to hybridize four types of redox-active quinone derivatives (QDs, Fig. 1) with activated carbon (AC) using the direct method (Scheme 1b) without heating. Tetramethyl-1,4-benzoquinone (TMBQ) and 2,6-di-*tert*-butyl-1,4-benzoquinone (DBBQ) are alkylbenzoquinones, and hybrids consisting of these alkylbenzoquinones and AC have been shown to exhibit high performance as electrochemical capacitor electrodes.[19,20] In addition to these alkylbenzoquinones, we examine phenylbenzoquinone (PBQ) and naphthoquinone (NQ) to expand the variety of QDs for preparing high-performance electrode materials. The resulting hybrids exhibit high performance as electrochemical capacitor electrodes, prepared *via* an ultimately simplified synthesis method.

2. Experimental

2.1. Materials and synthesis

KOH-activated carbon (AC; MSC30, Kansai Coke & Chemicals Co., Ltd.) was used as received. Tetramethyl-1,4-benzoquinone (TMBQ; Sigma-Aldrich), 2,6-di-*tert*-butyl-1,4-benzoquinone (DBBQ; Sigma-Aldrich), phenylbenzoquinone (PBQ; Tokyo Chemical Industry Co., Ltd.), and naphthoquinone (NQ; FUJIFILM Wako Pure Chemical Corp.) were crushed in a mortar before use. In a preliminary experiment, approximately 100 mg of AC was dried at 150 °C under vacuum for 1 h, after which it was mixed with the QD at 2000 rpm for 1 min using a planetary centrifugal mixer (ARE-310, THINKY). The mixture was stored in a 10 mL glass vial under N_2 at 25 °C until adsorption of the QD was complete. The QD loadings were 1 and 3 mmol per gram of AC. The resulting hybrids are denoted as AC/X (Y), where X indicates the type of QD and Y the millimolar amount of QD per gram of AC. In subsequent experiments, the amount of water adsorbed in AC, determined by vacuum drying in the preliminary experiment, was taken into account when weighing undried AC and QD for hybridization. YP-50F activated carbon, derived from coconut shell and prepared by steam activation, was purchased from Kuraray Co. and used as received.

2.2. Characterization

X-ray diffraction (XRD) analysis was performed on a Shimadzu XRD-6100 using Cu Kα radiation (λ = 1.5418 Å) at 30 kV and 20 mA. Raman spectra were collected with a Renishaw inVia Raman microscope equipped with a 532 nm excitation laser (laser power: 0.1 mW; spot diameter: ~1 μm). Differential scanning calorimetry (DSC) was conducted on a Shimadzu DSC-60 plus to determine the melting temperatures and enthalpies of the QDs. For DSC measurements, the QDs were sealed in an Al cell and heated at 1 °C min^{-1}. Thermogravimetric and differential thermal analyses (TG-DTA) were performed on a Shimadzu DTG-60H under a N_2 atmosphere (100 mL min^{-1}) at a heating rate of 10 °C min^{-1}.

N_2 adsorption–desorption measurements were carried out at −196 °C using an ASAP 2020 (Micromeritics). The Brunauer–Emmett–Teller (BET) specific surface area was determined from

adsorption data in the relative pressure range of P/P_0 = 0.05–0.20. The micropore volume was evaluated using the Dubinin–Radushkevich method, and the total pore volume was obtained from the adsorbed N_2 at P/P_0 = 0.96. The mesopore volume was calculated as the difference between the total and micropore volumes.

2.3. Electrochemical measurement

Electrochemical measurements were carried out at 25 °C using both three-electrode and coin cells with aqueous 1 M H_2SO_4 electrolyte. Detailed procedures for electrode preparation and apparatus descriptions are provided in our previous reports.[17,19]

Briefly, AC or AC/QD hybrids were mixed with carbon black (CB; DENKA BLACK Li, Denka Co., Ltd.) and polytetrafluoroethylene (PTFE; DuPont) at an AC/CB/PTFE mass ratio of 18 : 1 : 1. Because the QDs were adsorbed within the AC pores without expansion of the AC particle volume, the QD mass was excluded in calculating the AC content.[26] The resulting mixture was formed into 12 mm square sheets containing 8.5 mg of AC, yielding uniform electrode thickness, and sandwiched between stainless-steel mesh (100 mesh, Nilaco) under controlled conditions (30 MPa, 150 s) using a compact universal/tensile tester (EZ-LX, Shimadzu). Counter electrodes were prepared using AC in the same manner, except using 20 mg of the electrode sheet. A saturated KCl Ag/AgCl electrode served as the reference. CR2032-type coin cells were assembled from the electrode sheets together with a negative case, a Whatman glass microfiber filter (GF/D) separator, a spacer, a wave spring washer, and a positive case. Prior to measurement, electrodes were conditioned in electrolyte solution under vacuum for 1 h.

In the three-electrode cell, cyclic voltammetry (CV) was performed at 1 mV s^{-1} in the potential range of −0.1 to 0.8 V (*vs.* Ag/AgCl). Electrochemical impedance spectroscopy (EIS) was then conducted at the anodic peak potentials of the QDs, followed by galvanostatic charge/discharge (GCD) tests. In the coin cell configuration, CV was first performed at 1 mV s^{-1} within a cell voltage window of 0.8 V, followed by GCD measurements and cycling at 2 A g^{-1}. Leakage current was recorded for 2 h after charging a newly assembled cell at 2 A g^{-1} to 0.8 V, and self-discharge was measured immediately after the leakage current measurement.

The calculation methods for the following parameters are described in our previous work:[19] volumetric current (I_v), gravimetric capacitance (C_g), volumetric capacitance (C_v), gravimetric energy density, gravimetric power density, volumetric energy density, and volumetric power density.

2.4. Density and volume resistivity measurement

An electrode sheet containing approximately 100 mg of AC was prepared for density measurements of both AC and the AC/QD hybrids. The sheet was pressed into a pellet (ϕ = 13 mm) using a Shimadzu mold under the same conditions as for electrode preparation. The pellet thickness and mass were precisely determined using an autocollimator (DIGIMICRO MF-501, Nikon) and a microbalance, respectively, to calculate the density. The theoretical electrode densities of the AC/QD hybrids (ρ^{theo}, g cm^{-3}) were calculated from the experimental electrode density of AC and the weight percentages of the QDs, according to the following equation:[27]

$$\rho^{theo} = \rho_{AC}^{ex}\left(\frac{90}{100 - Z} + 0.1\right)$$

where ρ_{AC}^{ex} (g cm^{-3}) is the experimental electrode density of AC (0.326 g cm^{-3}),[16] and Z denotes the weight percentage of QDs in the sample.

Volume resistivity (R_V, Ω cm) was measured on the same pellets used for the density measurements with a low-resistivity meter (Loresta-GXII MCP-T710, Nittoseiko Analytech Co., Ltd.) equipped with a PSR prove (RMH504) and a probe stand (MCP-STD).

3. Results and discussion

3.1. Structural characterization

The hybridization of AC with QDs was achieved by a remarkably simple procedure, without the use of organic solvents or specialized apparatus. AC was mixed with QDs and kept at 25 °C until adsorption was complete (Scheme 1b). Since the QDs used in this study (Fig. 1) are crystalline solids at room temperature, they were ground into fine particles prior to use; the adsorption rate was found to depend on both temperature and particle size (Fig. S1, *vide infra*). KOH-activated AC employed in this study exhibited a BET specific surface area of 3160 m^2 g^{-1}, with pore sizes ranging from micropores to mesopores up to ~4 nm (*vide infra*). The QDs investigated were TMBQ, DBBQ, PBQ, and NQ (Fig. 1).

Adsorption of the QDs on AC can be readily confirmed by XRD analysis.[15,17–21] Fig. 2 presents the XRD patterns of AC, QDs, the AC–QD mixtures before completing adsorption, and the AC/QD hybrids (*i.e.*, after adsorption). The XRD pattern acquisition time from 5° to 50° required approximately 70 min, during which TMBQ, DBBQ, and NQ were rapidly adsorbed. To account for the rapid adsorption of these QDs on AC, the XRD measurement was limited to a narrower range for the mixtures. The QDs exhibit distinct diffraction peaks originating from their crystalline structures in the XRD patterns (Fig. 2a–d). In contrast, AC shows no sharp peaks but displays a weak and broad reflection at around 44°, corresponding to the carbon 10 diffraction, while the 002 diffraction at approximately 26° is absent. This feature indicates that the AC possesses a highly activated structure. If QDs were not adsorbed onto AC, the XRD patterns of the AC–QD mixtures would simply show a superposition of the characteristic peaks of both QDs and AC.[28,29] Indeed, before adsorption, the XRD patterns of the AC–TMBQ (Fig. 2a), AC–PBQ (Fig. 2c), and AC–NQ mixtures (Fig. 2d) exhibited QD-derived peaks. In contrast, the AC–DBBQ mixtures, measured immediately after mixing, showed no distinct peaks (Fig. 2b), while the adsorption of TMBQ and NQ was completed within 10–20 min (Fig. 2a and d). By

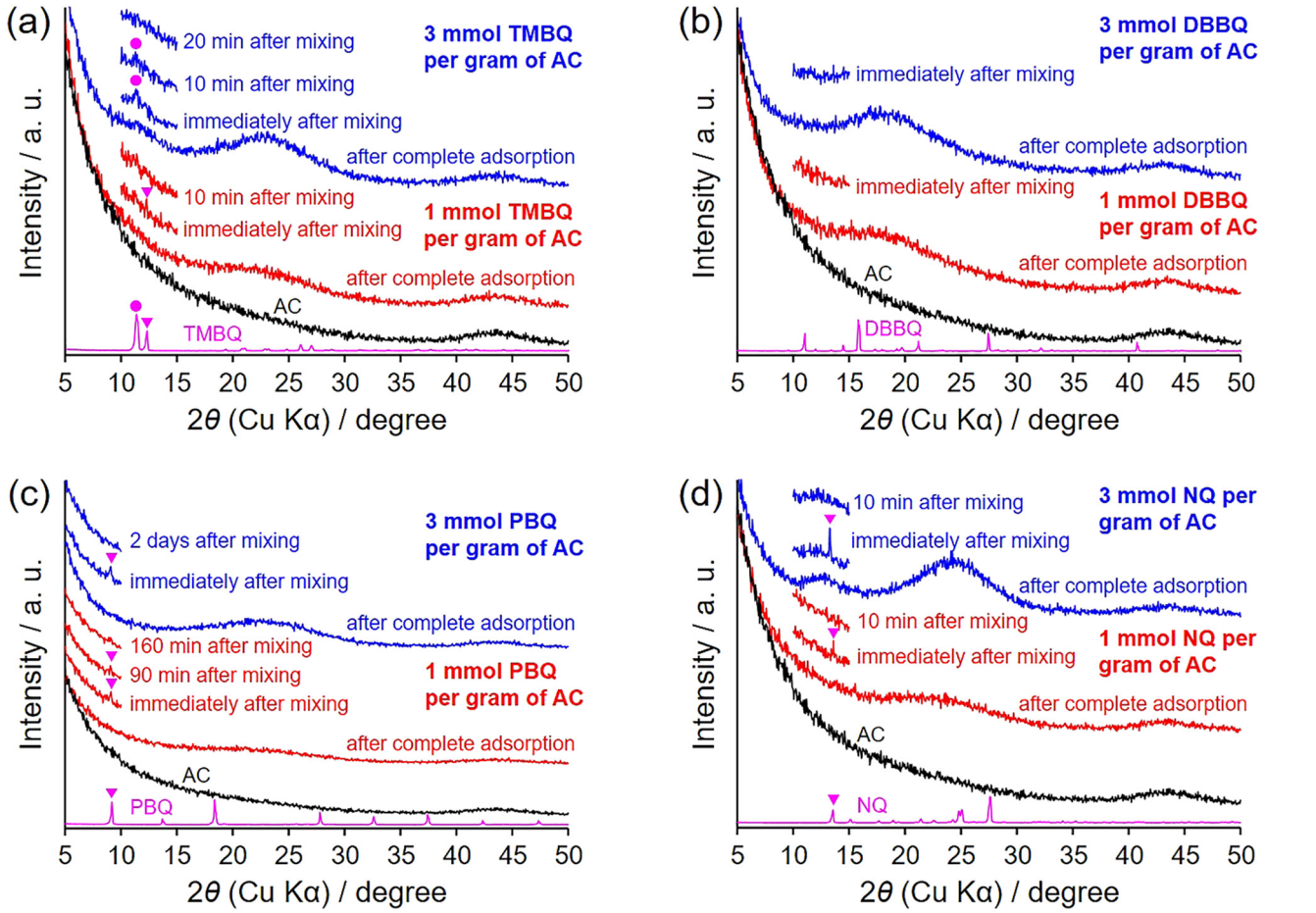

Fig. 2 XRD patterns of AC, QDs, their mixtures at various adsorption times, and the AC/QD hybrids (after complete adsorption). The QDs used are (a) TMBQ, (b) DBBQ, (c) PBQ, and (d) NQ.

comparison, PBQ required as long as 2 days to achieve complete adsorption, yielding AC/PBQ (3).

The slower adsorption of PBQ relative to the other QDs was also evident when the QD loading was increased (Fig. S2). Additional experiments using PBQ showed that the adsorption behaviour was not significantly affected by mixing time (1–10 min) or container geometry, whereas insufficient mixing slowed the adsorption process (Fig. S3). These results indicate that homogeneous mixing between the QD crystals and AC particles is the primary factor governing the adsorption rate. The rapid adsorption observed in the direct method, in which complete adsorption occurred within a very short time even at 25 °C, is highlighted by comparison with the indirect method (Scheme 1a). In the indirect method, adsorption of 1 and 3 mmol of TMBQ or DBBQ per gram of AC was completed within 1 h and more than 12 h, respectively, at 100 °C, whereas at 25 °C the adsorption of 1 mmol of DBBQ required approximately 3 days (Fig. S4).

After adsorption was completed, all AC/QD hybrids displayed a broad peak, with the peak intensity increasing as the QD content increased. This observation suggests that the QDs interact with the carbon surface through π–π interactions,[19] which typically occur at distances of ~3.2 Å for QDs[30] and ~3.2–3.6 Å for benzene and related derivatives on graphene surfaces.[31,32] However, the distances derived from the peak maxima in the XRD patterns, calculated using Bragg's law, were somewhat larger, ranging from 3.8 to 4.7 Å, and increased in the order NQ < PBQ < TMBQ < DBBQ. This discrepancy can be attributed to the structural nature of activated carbons: unlike flat graphene, the pore walls are curved and defective, so adsorbed molecules experience weaker and less uniform π–π interactions, effectively shifting the average wall–molecule separation to longer values.[33] In addition, while NQ is a rigid planar molecule, PBQ, although nominally planar due to π-electron delocalization, can undergo phenyl-quinone rotation within the confined pores, leading to a slightly greater separation. For TMBQ and DBBQ, the progressive increase in distance is dominated by steric hindrance from the bulkier alkyl substituents, which act as spacers or induce molecular tilt under slit-pore confinement.[32,33] Accordingly, the XRD-derived distances follow the order NQ < PBQ < TMBQ < DBBQ.

Fig. 3a shows the Raman spectra of the AC/QD hybrids with the higher loading level (3 mmol per gram of AC) together with that of pristine AC. No significant difference was observed in the intensity ratio of the D and G bands (I_D/

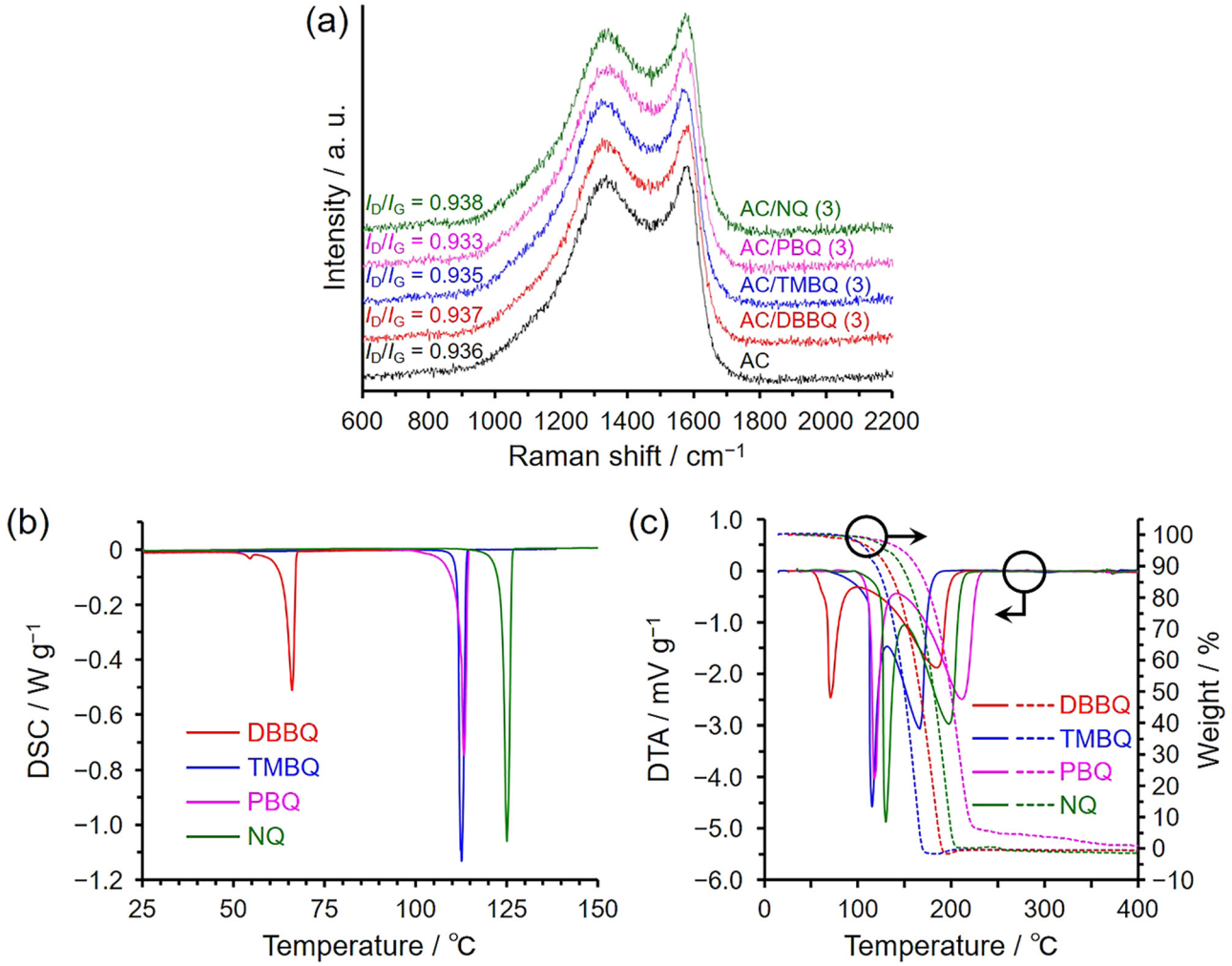

Fig. 3 (a) Raman spectra of the AC/QD hybrids (excitation wavelength: 532 nm). (b) DSC and (c) TG-DTA curves of the QDs. The heating rates for the DSC and TG-DTA measurements were 1 and 10 °C min^{-1}, respectively.

I_G = 0.933–0.938), indicating that the hybridization did not induce structural collapse of the AC pores and that the QDs were incorporated through physical interactions.[34] This is supported by the fact that AC and the AC/QD hybrids did not exhibit a significant difference in volume resistivity (*vide infra*), which does not depend on the shape or thickness of the material, simultaneously corroborating the absence of charge transfer between AC and QDs. Hydrogen-bonding, electrostatic, hydrophobic, and π–π interactions play an important role in the interaction with graphene oxide[35–37] and graphene.[38–40] Unlike graphene oxide, hydrogen-bonding and electrostatic interactions are not dominant for the interaction between AC and the QDs. This is because the QDs lack charged or polar functional groups, and the oxygen content of AC is much lower than that of graphene oxide (2.2 wt%; determined by temperature-programmed desorption analysis,[41,42] see Fig. S5). Notably, because adsorption was conducted in the gas phase, interfacial phenomena such as hydrophobic interactions, which are typical in liquid environments, did not contribute to the adsorption process. Consequently, π–π interactions[34,43–45] between the QDs and AC became the decisive factor governing adsorption.

Fig. 3b and c show the DSC and TG-DTA results of the QDs, respectively. As shown in Fig. 3b, DSC analysis provided the fusion temperatures (T_{fus}) and enthalpies (ΔH_{fus}) of the QDs. In contrast, TG-DTA analysis yielded T_{fus} and vaporization temperatures (T_{vap}), together with the corresponding enthalpies (ΔH_{fus} and ΔH_{vap}) (Fig. 3c). As shown in Fig. 3c, the fusion and vaporization peaks overlap in the DTA patterns; however, ΔH_{vap} can be estimated from the difference between the total endotherm (ΔH_{fus} + ΔH_{vap}) obtained by DTA and ΔH_{fus} measured by DSC. Note that T_{fus} determined by TG-DTA are 6–9 °C higher than those obtained by DSC because the heating rate of TG-DTA (10 °C min^{-1}) was higher than that of DSC (1 °C min^{-1}). A higher heating rate generally produces sharper peaks, which facilitates a more accurate evaluation of enthalpies, but it also shifts the measured T_{fus} and T_{vap} to higher values. Therefore, the TG-DTA measurements in this study were performed at 10 °C min^{-1}, whereas the DSC measurements were conducted at 1 °C min^{-1}, since sufficiently sharp peaks were

Table 1 Thermal parameters obtained from DSC and TG-DTA measurements

QDs	M. W.[a] (g mol^{-1})	T_{fus}[b] (°C)	ΔH_{fus}[c] (kJ mol^{-1})	$\Delta H_{fus} + \Delta H_{vap}$[d] (kJ mol^{-1})	ΔH_{vap}[e] (kJ mol^{-1})
TMBQ	164.20	112.6	16.8	149.5	132.7
DBBQ	220.31	66.0	18.3	177.6	159.2
PBQ	184.19	113.3	21.2	178.6	157.4
NQ	158.15	124.9	20.4	164.2	143.8

[a] Molecular weight. [b] Melting temperature (T_{fus}) determined by DSC. [c] Fusion enthalpy (ΔH_{fus}) determined by DSC. [d] Fusion enthalpy (ΔH_{fus}) and evaporation enthalpy (ΔH_{vap}) determined by TG-DTA. [e] ΔH_{vap} calculated as the difference between the total endotherm obtained from TG-DTA and ΔH_{fus} determined by DSC.

obtained even at this lower rate and an accurate determination of T_{fus} was desired. Table 1 summarizes the thermal analysis data obtained from TG-DTA and DSC measurements. In the XRD measurements, the order of adsorption affinity was PBQ < TMBQ < NQ < DBBQ; however, no clear correlation with the adsorption tendency of the QDs was observed in the respective thermal analysis data shown in Table 1. The ease of mass loss associated with vaporization observed in the TG profiles decreased in the order TMBQ > DBBQ > NQ > PBQ, whereas the corresponding peak temperatures increased in the order TMBQ < DBBQ < NQ < PBQ. These correlations, however, did not correspond to the adsorption affinity.

The molecular weights and sizes of the QDs are not directly responsible for the adsorption affinity; therefore, the driving force of adsorption is likely also correlated with entropy changes. In this case, the transition of the QD molecules from an ordered crystalline state to a more dispersed state within the AC pores results in an increase in system entropy ($\Delta S > 0$). Unlike the negative ΔS typically observed in gas adsorption onto porous materials, such as in N_2 adsorption–desorption measurements, this fundamental difference explains why the entropy change upon adsorption is positive in this study. In this process, the intermolecular interaction among QD molecules[46] is replaced by interactions between the carbon pore surfaces and QD molecules through π–π interactions.[34,43–45] It has been reported that the adsorption of molecules from water onto carbon nanotube surfaces is driven by both enthalpy and entropy changes of the adsorbates and surrounding water molecules.[33] In such systems, the enthalpy change is not necessarily the dominant factor compared with the entropy change, as hydrophobic molecules disrupt the structured water shell upon adsorption and thereby increase the entropy of the system. In the present case, the adsorption is simpler due to the absence of solvents. However, the adsorption enthalpy cannot be experimentally measured because QD adsorption onto AC proceeds immediately upon mixing. Factors that influence the adsorption rate include the particle size of the QDs and the adsorption temperature (Fig. S1). Smaller particle sizes increase the contact area between QDs and AC, which accelerates the adsorption process, while higher temperatures enhance the $-T\Delta S$ contribution, favouring a decrease in ΔG ($= \Delta H - T\Delta S$). Thus, adsorption is more thermodynamically favoured at higher temperatures.

N_2 adsorption–desorption isotherms of AC, AC/TMBQ (1), and AC/TMBQ (3) are shown in Fig. 4a. Because the results of the other AC/QD hybrids showed the identical tendency to those of the AC/TMBQ hybrids, their results are summarized in the SI (Fig. S6–S8). Note that the amount of adsorbed N_2 was calculated per gram of AC for the hybrids and the normalized values are plotted in the figure. If the QDs were not adsorbed in the pores and all QD molecules deposited on the outer surface of the AC particles, the normalized isotherm of the hybrids would not show a difference from that of AC, owing to the negligible surface areas of the QDs in comparison to that of AC. AC shows micropore filling below P/P_0 of 0.05 and adsorption up to P/P_0 of 0.4, suggesting that the AC has micropores and small mesopores. In comparison to the AC, the adsorbed amount of N_2 decreases with increasing QD content in the P/P_0 range of 0 to 0.4 (Fig. 4a and S6–S8), suggesting that QDs were adsorbed by both micropores and mesopores. The pore size distribution of AC indicates the presence of micropores and mesopores of 2–4 nm (Fig. 4b). The pore size distributions of the hybrids exhibit almost the same shape as that of AC (Fig. 4b and S6–S8). However, these results may involve some errors because the pore size distributions were calculated assuming a carbon slit-pore model, whereas the actual pore structures of the hybrids are likely to deviate from the model due to the presence of QDs within the pores.

Table 2 summarises the BET specific surface areas and pore volumes of pristine AC and the AC/QD hybrids, in addition to their normalized values. The dependences of the normalized BET specific surface areas and pore volumes on the QD contents per gram of AC are presented in Fig. 4c and S6–S8. As well as the normalized BET specific surface areas, the normalized micropore and total pore volumes of the hybrids decrease linearly with increasing TMBQ content, as evidenced by the high coefficients of determination (R^2 = 0.990–0.999). Notably, despite being obtained by different calculation methods, all three parameters exhibit this linear decrease, underscoring the robustness of the trend. This result indicates that the QDs were not preferentially adsorbed in either micropores or mesopores but rather distributed equally across both pore types. In contrast to N_2 micropore filling at −196 °C, these findings suggest that QD molecules diffuse evenly over both micropore and mesopore surfaces. Before adsorption, the QD molecules interact in the crystalline phase. Upon mixing

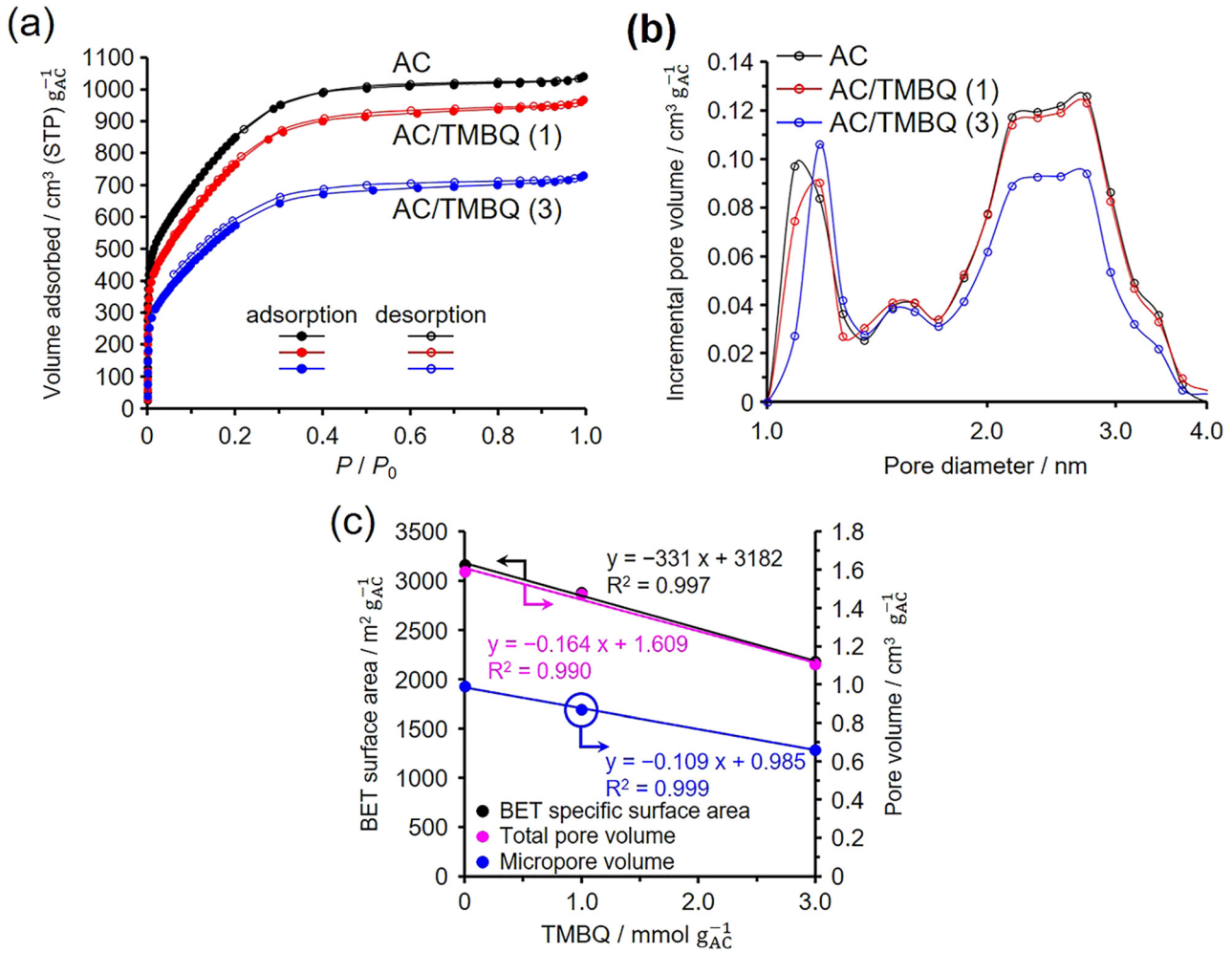

Fig. 4 N_2 adsorption–desorption isotherms and pore characteristics of AC and the AC/QD hybrids: (a) N_2 adsorption–desorption isotherms, (b) pore size distributions calculated by the DFT method assuming slit-shaped carbon pores, and (c) dependence of BET specific surface area and pore volumes on the TMBQ content. The values are expressed per gram of AC.

Table 2 BET specific surface areas and pore volumes of AC and the AC/QD hybrids

Samples	S_{BET} [a] $(m^2\ g^{-1})/(m^2\ g_{AC}^{-1})$	V_{total} [b] $(cm^3\ g^{-1})/(cm^3\ g_{AC}^{-1})$	V_{micro} [c] $(cm^3\ g^{-1})/(cm^3\ g_{AC}^{-1})$	V_{meso} [d] $(cm^3\ g^{-1})/(cm^3\ g_{AC}^{-1})$
AC	3160	1.59	0.99	0.60
AC/TMBQ (1)	2470/2880	1.26/1.47	0.75/0.87	0.52/0.60
AC/TMBQ (3)	1460/2180	0.74/1.11	0.44/0.66	0.30/0.45
AC/DBBQ (1)	2230/2730	1.13/1.38	0.67/0.82	0.46/0.57
AC/DBBQ (3)	1050/1740	0.54/0.89	0.31/0.52	0.22/0.37
AC/PBQ (1)	2470/2920	1.25/1.48	0.76/0.91	0.49/0.58
AC/PBQ (3)	1500/2320	0.76/1.17	0.46/0.71	0.30/0.46
AC/NQ (1)	2570/2970	1.26/1.46	0.81/0.93	0.46/0.53
AC/NQ (3)	1720/2530	0.87/1.28	0.54/0.80	0.33/0.48

[a] BET specific surface area (S_{BET}). [b] Total pore volume (V_{total}). [c] Micropore volume (V_{micro}) calculated by the Dubinin–Radushkevich (DR) method. [d] Mesopore volume (V_{meso}) calculated as the difference between V_{total} and V_{micro}. For the hybrid samples, the values on the left of "/" are expressed per total sample weight, and those on the right are expressed per gram of AC.

with AC at 25 °C, the QD molecules located at the crystal surfaces and in contact with the external surfaces of the AC particles rapidly diffused onto the AC surfaces. These molecules were adsorbed beginning at the pore entrances and subsequently diffusing into both micropores and mesopores. At this stage, the dominant interactions of the QD molecules were

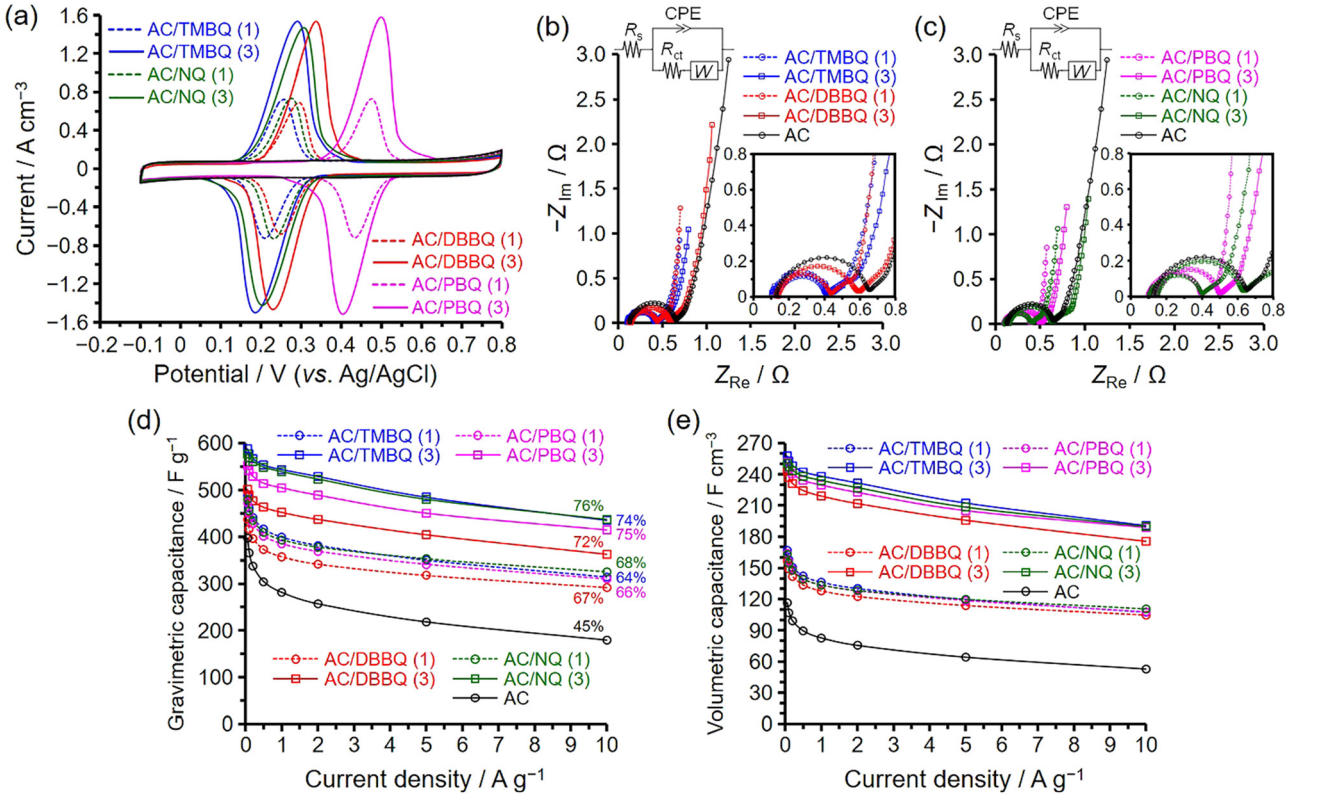

Fig. 5 Electrochemical characteristics of AC and the AC/QD hybrids measured at 25 °C in 1 M H_2SO_4 using a three-electrode cell: (a) cyclic voltammograms recorded at 1 mV s^{-1}, (b and c) Nyquist plots obtained at 0.5 V *vs.* Ag/AgCl for AC and at the anodic peak potentials for the AC/QD hybrids, with inset showing the equivalent circuit used for fitting (R_s + CPE // (R_{ct} + W_d)), and (d and e) dependence of (d) gravimetric and (e) volumetric capacitances on current density determined by GCD measurements. The potential range for the CV (a) and GCD (d and e) tests was −0.1 to 0.8 V (*vs.* Ag/AgCl).

replaced, shifting from intermolecular interactions to interactions with the carbon pore surfaces.

3.2. Electrochemical capacitor performance of the AC/QD hybrids measured using a three-electrode cell

Fig. 5 shows the results obtained with the three-electrode cell at 25 °C. The measurement sequence was CV, EIS, and GCD, and the potential range of CV and GCD was −0.1 to 0.8 V (*vs.* Ag/AgCl). Electrode densities were experimentally determined and compared with theoretical values (Table 3). The theoretical electrode densities were calculated using the electrode density of AC, assuming that the QDs were incorporated within the AC pores without volume expansion of the AC particles (for details, see the Experimental section).[17] The experimental electrode densities were in good agreement with the theoretical values,

Table 3 Physical and electrochemical parameters, including EIS-derived resistive components, of AC and the AC/QD hybrid electrodes

Samples	QD content (wt%)	Electrode density ρ^{exa}/ρ^{theo} [b] (g cm^{-3})	R_v [c] (Ω cm)	Utilization efficiency [d] (%)	Capacitance retention [e] (%)	R_s [f] (Ω)	R_{ct} [g] (Ω)	R_{ct}/n_{QD} [h] [Ω $mmol^{-1}$]	W_d [i] [Ω]
AC	—	0.33	2.15	—	45	0.13	0.51	—	1.31
AC/TMBQ (1)	14.1	—	—	90	64	0.14	0.26	0.26	0.61
AC/TMBQ (3)	33.0	0.49/0.47	2.19	94	74	0.09	0.34	0.11	0.79
AC/DBBQ (1)	18.1	—	—	80	67	0.12	0.30	0.30	0.17
AC/DBBQ (3)	39.8	0.54/0.52	2.11	86	72	0.14	0.43	0.14	0.62
AC/PBQ (1)	15.6	—	—	85	66	0.10	0.30	0.30	0.14
AC/PBQ (3)	35.6	0.49/0.49	2.11	87	75	0.14	0.34	0.11	0.47
AC/NQ (1)	13.7	—	—	91	68	0.10	0.30	0.30	0.55
AC/NQ (3)	32.2	0.48/0.47	2.13	90	76	0.15	0.47	0.16	0.70

[a] Experimental electrode density (ρ^{ex}). [b] Theoretical electrode density (ρ^{theo}) calculated from the experimental electrode density of AC and the weight percentage of QD. [c] Volume resistivity (R_v). [d] Utilization efficiency of QD calculated from the voltammograms recorded by CV at 1 mV s^{-1}. [e] Capacitance retention calculated from the capacitance at 10 A g^{-1} relative to that at 0.05 A g^{-1}. [f] Bulk solution resistance (R_s), obtained from EIS fitting. [g] Charge-transfer resistance (R_{ct}) obtained from EIS fitting. [h] QD-amount-normalized charge-transfer resistance (R_{ct}/n_{QD}), obtained from EIS fitting. [i] Diffusion-related parameter associated with the Warburg element (W_d), obtained from EIS fitting.

confirming that the QDs were accommodated within the AC pores. Therefore, the mass of AC in the electrodes of the AC/QD hybrids was the same as that of the pristine AC, regardless of the QD content; accordingly, the electrode thicknesses were constant for both AC and the AC/QD hybrids.[15,17,18] In addition, the volume resistivities of the electrodes, which remain constant irrespective of shape or thickness, were analysed using a four-probe resistivity measurement and are summarized in Table 3. The volume resistivities of AC and the AC/QD hybrids were nearly identical, indicating that the incorporation of redox-active QDs into the AC pores did not deteriorate the electronic conductivity. This result suggests that direct charge transfer between the QDs and the AC framework was negligible under non-electrochemical conditions, that is, in the absence of an applied potential in electrolyte solutions, consistent with the Raman spectra of AC and the AC/QD hybrids (Fig. 3a). Therefore, the resistance contribution associated with electrode thickness was constant for both AC and the AC/QD hybrids, ensuring a fair comparison of electrochemical capacitor performance. For these reasons, the current values in the voltammograms (Fig. 5a) and the capacitances in Fig. 5e are plotted on a per-volume basis.

The voltammogram of AC is a typical rectangular shape (Fig. 5a), characteristic of EDLC behaviour. Meanwhile, the AC/QD hybrids show a distinct peak with peak intensity being higher for the hybrids with a higher QD content. For comparison, control electrodes prepared by physically mixing each QD with conductive carbon black and PTFE binder were evaluated under identical conditions (Fig. S9). The redox peak potentials of these control electrodes are generally consistent with those of the corresponding AC/QD hybrids, although minor shifts are observed for some derivatives. These results indicate that hybridization within AC pores does not significantly alter the intrinsic redox potentials of the QDs. The current observed in the voltammograms can be separated into two components: one attributed to the formation of the electric double layer (EDL), and the other to the reversible redox reactions of the QDs. The plateau observed in the voltammograms is characterized by a constant current arising from the EDL formation, while the difference between the peak current and this EDL-derived current can be attributed to the redox reactions of the QDs. Although the QDs were hybridized within the AC pores, the EDL-derived current remains clearly observable in the voltammograms, as evidenced by the small difference in EDL-derived current between AC and the AC/QD hybrids. The AC/QD hybrids with a higher QD loading show only a slightly lower EDL-derived current compared with those with lower loading. Furthermore, cyclic voltammograms recorded after the GCD measurements exhibit nearly identical EDL-derived currents to those obtained before cycling (Fig. S10). These results suggest that ion conduction within the AC pores, as well as EDL formation, is not significantly impeded by QD hybridization, and that the electrochemically accessible surface area is largely preserved.[19,26,47,48] This interpretation is consistent with the retained micropore and mesopore volumes observed by N_2 adsorption–desorption measurements (Table 2). The distinct peaks in the voltammograms suggest that the reversible redox reactions of the QDs proceeded with low charge-transfer resistance (*vide infra*). The utilization efficiency of the QDs was defined as the ratio of the experimentally obtained anodic charge to the theoretical charge calculated from the amount of hybridized QDs, assuming a two-electron redox process.[48] The experimental charge was determined by integrating the redox peak after subtracting the EDL-derived current contribution in the voltammogram recorded at 1 mV s^{-1} (Fig. S11). The resulting values are summarized in Table 3. The utilization efficiencies are as high as 80–94%, and such high utilization efficiencies are explained by the large contact area between the hybridized QDs and conductive carbon surfaces. Voltammograms recorded at higher sweep rates revealed that the AC/QD hybrids exhibited trends consistent with those observed in the GCD results (*vide infra*), and the potential difference between anodic and cathodic peaks increased with increasing sweep rate (Fig. S12). A Trasatti-type analysis was performed to further assess the capacitive contributions based on scan-rate-dependent cyclic voltammograms (1–50 mV s^{-1}) (Fig. S13).[49] However, the resulting Trasatti plots did not exhibit a well-defined linear region across the investigated scan-rate window; therefore, a reliable quantitative separation of EDLC and pseudocapacitive contributions could not be obtained. Electrochemical impedance spectroscopy further indicates that the charge-transfer resistance remains low (*vide infra*), suggesting that the observed scan-rate dependence of the cyclic voltammograms primarily originates from mass transport and proton-transfer limitations rather than sluggish electron transfer.

Fig. 5b and c present the Nyquist plots obtained from EIS measurements for the AC/QD hybrids and pristine AC. The resistance components determined by EIS include bulk solution, contact, charge-transfer, and diffusion resistances. The contact resistance arises from the interparticle interfaces among AC particles as well as from the interfaces between the AC particles and the current collector. All electrodes were fabricated under strictly controlled conditions (for details, see the Experimental section). Moreover, since the QDs were hybridized within the AC pores, neither the particle volume of AC nor the volume resistivity of the electrodes was altered (*vide supra*). Therefore, the bulk solution and contact resistances remain unchanged between the AC/QD hybrid and pristine AC electrodes, and any difference in overall cell resistance can be attributed to the charge-transfer and diffusion resistances.

The semicircle observed at high frequencies increases in size with increasing charge-transfer and contact resistances,[50,51] although the difference in contact resistance is negligible for both AC and the AC/QD hybrids. At low frequencies, the locus deviates from the vertical axis as the diffusion resistance increases.[52] For quantitative comparison, the Nyquist plots were fitted using an equivalent circuit to extract the solution resistance (R_s), the charge-transfer resistance (R_{ct}), and a diffusion-related parameter associated with the Warburg element (W_d). In addition, the QD-amount-normalized charge-transfer resistance (R_{ct}/n_{QD}) was calculated

to enable comparison across different QD types and loading levels, and the resulting values are summarized in Table 3. The fitted solution resistance values were comparable among all electrodes (0.09–0.15 Ω), while the charge-transfer resistance of the AC/QD hybrids remained in a relatively low range (0.26–0.47 Ω). The AC/QD hybrids with higher QD loadings exhibit enlarged semicircles, indicating that a larger QD content increases the charge-transfer resistance owing to the greater contribution from redox charge transfer. Nevertheless, the charge-transfer resistance of the AC/QD hybrids remains lower than that of pristine AC (Table 3). The QD molecules are in good contact with the conductive carbon surfaces within the AC pores; therefore, rapid charge transfer occurs through these extensive interfacial contacts. Consequently, the charge transfer associated with the QDs, rather than with the oxygen-containing functional groups of AC (Fig. S5), proceeds preferentially, resulting in a reduction in charge-transfer resistance (*vide infra*).[19,20,23,27] Because the QD-amount-normalized charge-transfer resistance decreases with increasing QD content (Table 3), the charge-transfer process per unit QD loading becomes more efficient at higher loadings. This trend suggests that the redox processes associated with the QDs progressively dominate over those originating from the oxygen-containing functional groups of AC (Fig. S5), indicating that charge transfer through QD–carbon interfaces becomes the primary pathway. The AC/QD hybrids do not exhibit an increase in diffusion resistance compared with AC because the QD content is not sufficiently large to impede ion transport within the pores.[19] This interpretation is consistent with the negligible difference in EDL-derived current values between the AC/QD hybrids and AC observed in the voltammograms (Fig. 5a). Furthermore, the N_2 adsorption–desorption results confirm that substantial micropore and mesopore volumes were retained in the AC/QD hybrids (Table 2). In addition to the EIS measurements performed at the anodic peak potential of the QD redox process for the AC/QD hybrids and at 0.5 V for pristine AC, EIS was also recorded at a potential outside the redox region (0 V, Fig. S14). Slight differences between the Nyquist plots obtained at the two potentials are also observed for pristine AC. In contrast, the Nyquist plots of the AC/QD hybrids show almost no discernible change with potential. This indicates that the impedance response is only weakly potential-dependent under the present conditions. Such behaviour suggests that interfacial electron transfer is sufficiently fast and that the overall response is dominated by transport and polarization effects in the porous electrode.

Fig. 5d and e show the dependence of the gravimetric and volumetric capacitances on current density, respectively. The gravimetric capacitances were obtained from the GCD curves (Fig. S15 and S16), and the volumetric capacitances were derived from these values using the electrode densities.[19] The percentages in Fig. 5d indicate the capacitance retentions at 10 A g^{-1} relative to those at 0.05 A g^{-1}. Note that the retentions calculated from gravimetric and volumetric capacitances are identical. AC exhibits a high gravimetric capacitance of 397 F g^{-1} with a capacitance retention of 45%, attributable to its large BET specific surface area (3160 m^2 g^{-1}) and the presence of mesopores smaller than 4 nm.[17,21] Although larger mesopores generally improve capacitance retention by reducing diffusion resistance,[53–55] they do so at the expense of lowering the BET specific surface area, which in turn reduces the capacitance.[18] Therefore, mesopores up to ~4 nm are advantageous for simultaneously achieving high capacitance and good capacitance retention. AC contains 2.2 wt% oxygen in the form of oxygen-containing functional groups (Fig. S5), whereas the QD-derived oxygen contents in the AC/QD hybrids are estimated from the QD loadings to be 2.6–6.5 wt%. The charge-transfer resistance of AC originates from these oxygen-containing functional groups and was higher than that of any AC/QD hybrid (Fig. 5b and c, Table 3); however, their contribution to capacitance enhancement is negligible compared with that of the QDs.[56]

Although the QD loadings were fixed at 1 and 3 mmol per gram of AC, the corresponding weight percentages of the QDs in the hybrids varied depending on their molecular weights (Table 3). Consequently, even when the number of adsorbed QD molecules and their utilization efficiencies are the same, the gravimetric capacitance decreases with increasing molecular weight (Fig. 5d). In contrast, the volumetric capacitance increases with QD content (Fig. 5e), regardless of molecular weight, because the hybridized QDs maintained high utilization efficiencies irrespective of their loading. Moreover, the capacitance retention increases with QD content for all AC/QD hybrids (Table 3). This can be attributed to the superior charge–discharge mechanism of the QDs: their redox reactions provide faster and more efficient charge–discharge processes compared with EDL formation within the AC pores. The CV recorded after the GCD measurements (Fig. S10) exhibited nearly identical redox peak positions to those observed in the initial CV (Fig. 5a), indicating that the hybridized QDs remain electrochemically stable during the measurements and that their molecular structures are preserved under the present operating conditions. The reproducibility of the hybrid preparation was confirmed by preparing multiple independent batches under identical conditions, which showed consistent electrochemical behaviour (Fig. S17). To further verify the consistency between GCD and CV measurements, the capacitance derived from the GCD at 0.5 A g^{-1} was compared with that obtained from CV recorded at 1 mV s^{-1} within the same potential window (−0.1 to 0.8 V). Under these comparable time scales, the capacitance values were found to be in good agreement (Table S1), confirming the internal consistency of the electrochemical evaluation.

We previously reported high utilization efficiencies of TMBQ and DBBQ (87–91%).[19] When 2 mmol of TMBQ and 2 mmol of DBBQ were individually hybridized with the same AC by heating slightly below their melting temperatures *via* the direct method (Scheme 1b), the capacitance retentions at 10 A g^{-1} were 68–71%, and the electrochemical capacitor performances were essentially identical to those observed in

this study. As an additional experiment, 3 mmol of TMBQ and 3 mmol of DBBQ were individually hybridized with AC at 100 °C using the indirect method (Scheme 1a). In this method, the QDs were first vaporized and subsequently adsorbed within the AC pores in the vapor phase, and the adsorption required more than 12 h to complete (Fig. S4), in stark contrast to the direct method, in which adsorption was accomplished much more rapidly. The resulting hybrids exhibited electrochemical capacitor performances (Fig. S18) identical to those of AC/TMBQ (3) and AC/DBBQ (3) (Fig. 5), confirming that both the direct and indirect methods ultimately produce the same dispersion of QDs inside the AC pores. These results demonstrate that although Scheme 1a and b follow different adsorption pathways, they converge to the same final hybrid state, and they further highlight that direct molecular contact with AC particles significantly accelerates adsorption at room temperature, consistent with a mechanism driven by π–π interactions between QDs and the AC carbon surface. The slightly lower capacitance retention among the AC/QD hybrids containing 3 mmol of QDs per gram of AC was observed for AC/DBBQ (3), prepared by both the direct (Fig. 5d and e, Table 3) and indirect (Fig. S18) methods. This behaviour is attributed to the presence of two bulky *tert*-butyl groups in DBBQ, which hinder ion diffusion within the pores at high current densities.

To further assess the practical feasibility of this method, we examined whether the drying step of AC could be omitted prior to hybridization. AC/TMBQ (3) and AC/PBQ (3) were prepared without drying AC through the direct method at 25 °C. The amount of adsorbed water in AC was determined in a preliminary experiment (3.3 wt%), and AC was weighed on the basis of the measured adsorbed water content. Their electrochemical performances and adsorption behaviour did not show any significant difference (Fig. S19) from those shown in Fig. 2 and 5, and these hybrids were used for asymmetric coin cell measurements (*vide infra*) because of the largest potential difference between TMBQ and PBQ (Fig. 5a). Importantly, the water molecules remaining in the AC pores did not hinder the adsorption or redox reactions of the QDs, because the AC used in this study contains only a very small amount of adsorbed water (3.3 wt%) and is predominantly hydrophobic. In addition, since the electrochemical reactions of QDs necessarily require a proton-containing aqueous electrolyte, the presence of adsorbed water is not detrimental and can be considered acceptable. The amount of adsorbed water in AC remains constant as long as the storage conditions, such as humidity and temperature, are maintained. Therefore, the present hybridization method requires only weighing and mixing AC with the QDs, eliminating filtration, drying, heating, purification, and vacuum operations, as well as the use of solvents and specialized apparatus. Accordingly, this hybridization method is ultimately a simple, energy-efficient, and environmentally sustainable approach for preparing high-performance AC/QD hybrid electrodes.

3.3. Coin cell measurements

An asymmetric coin cell, denoted as AC/TMBQ (3)||AC/PBQ (3), was evaluated at a cell voltage of 0.8 V. Here, AC/TMBQ (3) and AC/PBQ (3) served as the negative and positive electrodes, respectively. The measurements were performed in the following sequence: CV, GCD, and finally a cycle test at 2 A g^{-1}. Among the QD combinations investigated, the redox potential difference between TMBQ and PBQ was the largest (Fig. 5a). In addition, the volumetric capacitance increased with QD loading while maintaining high capacitance retention. Therefore, AC/TMBQ (3) and AC/PBQ (3) prepared without drying AC (Fig. S19) were selected for cell fabrication. For comparison, a symmetric AC||AC cell was tested under identical conditions. The negative and positive electrodes of both cells contained the same mass of AC, which means that the electrode thickness was constant regardless of the presence or amount of QDs (*vide supra*). As shown in Fig. 6a, the symmetric AC||AC cell exhibited a nearly rectangular voltammogram, characteristic of electric double-layer behaviour. In contrast, the AC/TMBQ (3) (negative)||AC/PBQ (3) (positive) cell showed pronounced redox peaks and a substantially larger volumetric current, arising from the redox reactions of TMBQ and PBQ confined within the AC pores. Although TMBQ and PBQ were introduced into the electrodes in their quinone forms, partial reduction to the hydroquinone form is expected to occur upon immersion in the electrolyte, as evidenced by the initial voltammetric behaviour (Fig. S20). As discussed below (*vide infra*), during the first four CV cycles the electrochemical responses gradually evolve, and the redox peaks associated with TMBQ and PBQ become more distinct with increasing cycle number. This behaviour suggests that the redox-active states of the QDs are progressively established in the electrode during the initial activation process.

Fig. 6b shows the dependence of the gravimetric and volumetric capacitances on current density. The GCD measurements of the coin cells were performed up to a current density of 5 A g^{-1}, which corresponds to 10 A g^{-1} in the three-electrode configuration. The percentages and times in Fig. 6b represent capacitance retention relative to the values at 0.05 A g^{-1} and the corresponding charging times, respectively. For example, AC/TMBQ (3)||AC/PBQ (3) exhibits a volumetric capacitance 6.1 times higher than that of AC||AC at 1 A g^{-1} (Fig. 6b). In comparison, AC/TMBQ (3) and AC/PBQ (3) show 3.1- and 2.9-fold increases in volumetric capacitance at 2 A g^{-1}, respectively, in the three-electrode measurements (Fig. 5e). These results indicate that both TMBQ and PBQ contribute to the charge-storage process during the subsequent GCD measurements after the initial CV activation cycles. The volumetric capacitances of AC/TMBQ (3)||AC/PBQ (3) are 5.9–6.3 times higher than those of AC||AC below 5 A g^{-1}, with a capacitance retention of 71% at 2 A g^{-1}. This marked enhancement is attributed to the concerted redox reactions of TMBQ and PBQ at the negative and positive electrodes, respectively. However, the asymmetric AC/TMBQ (3)||AC/PBQ (3) cell exhibited a

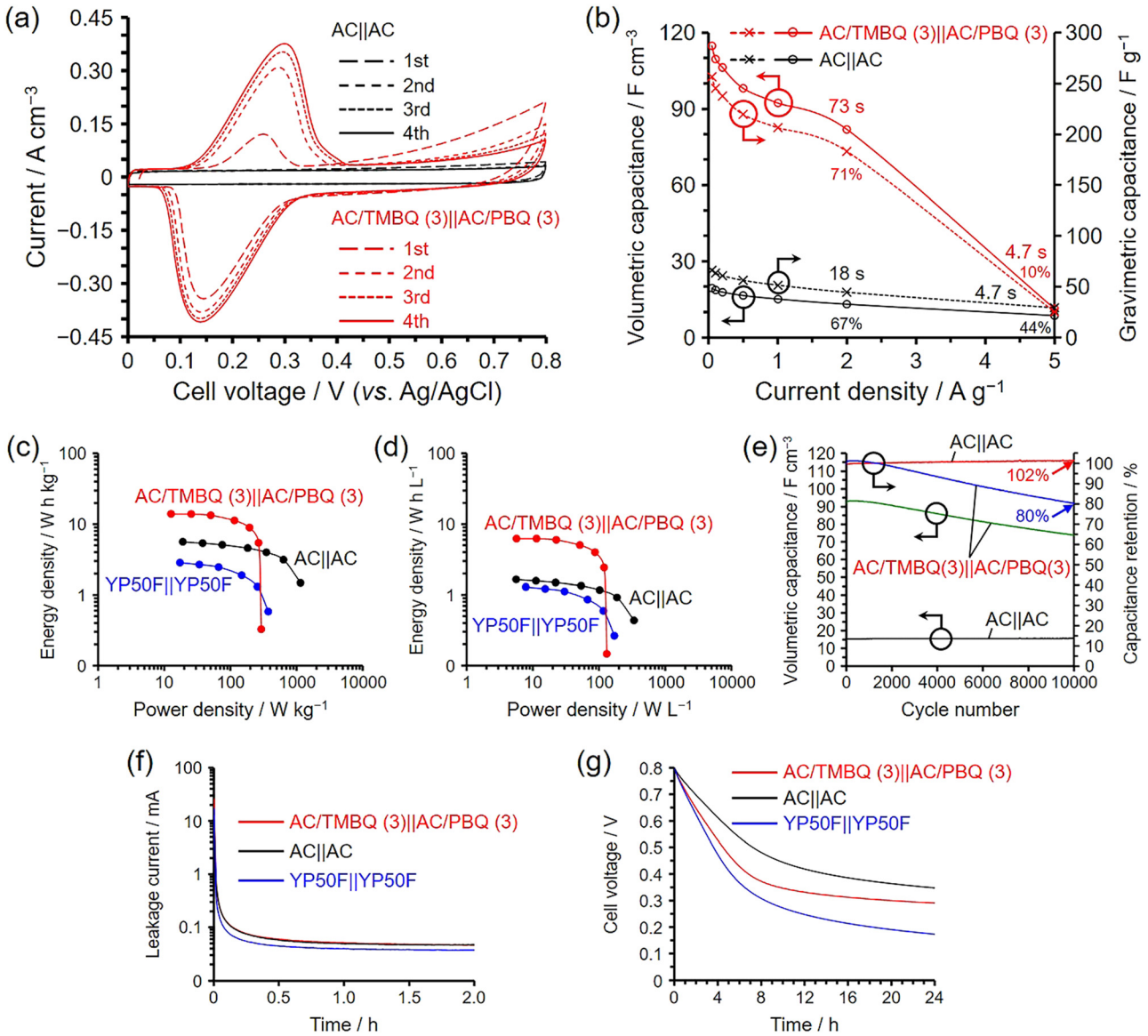

Fig. 6 Electrochemical performance of symmetric AC||AC and YP-50F||YP-50F coin cells and an asymmetric AC/TMBQ (3) (negative)||AC/PBQ (3) (positive) coin cell measured at 25 °C in 1 M H_2SO_4: (a) cyclic voltammograms recorded at 1 mV s^{-1}; (b) gravimetric and volumetric capacitances as a function of current density determined from GCD measurements; (c) gravimetric energy density as a function of gravimetric power density; (d) volumetric energy density as a function of volumetric power density; and (e) cycle performance measured at 2 A g^{-1}. (f) Leakage current as a function of time for 2 h recorded after charging at 2 A g^{-1} to 0.8 V. (g) Self-discharge curves (open-circuit voltage decay) measured immediately after the leakage current measurement. The cell voltage range for the CV and GCD tests was 0–0.8 V.

pronounced decrease in retention at 5 A g^{-1}. The GCD curves of AC in the three-electrode configuration exhibited triangular profiles without plateaus, which are typical of EDLC behaviour (Fig. S15a and b).[57] Consequently, this triangular shape was reflected in the GCD curves of the symmetric AC||AC cell, and the cell likewise displayed EDLC-type triangular profiles across all current densities without a plateau (Fig. S21a and b). In contrast, the asymmetric AC/TMBQ (3)||AC/PBQ (3) cell exhibited a distinct plateau from 0.05 to 2 A g^{-1}, whereas no plateau was observed at 5 A g^{-1} (Fig. S21c and d), indicating that the redox reactions of TMBQ and PBQ were limited at such high current density.

Three-electrode cell measurements provide information on electrochemical behaviour within a defined potential window rather than on the practical performance of electrochemical capacitors. In this study, the working electrode potentials were controlled from −0.1 to 0.8 V (*vs.* Ag/AgCl), corresponding to a range of 0.9 V (Fig. 5a). In contrast, two-electrode cell measurements, including coin cells, are controlled by the overall cell voltage, while the potential ranges of the negative and positive electrodes cannot be independently adjusted. Because the initial voltages of both the symmetric AC||AC and asymmetric AC/TMBQ (3)||AC/PBQ (3) cells were essentially zero, the initial potentials of their negative and positive

electrodes must have been nearly identical. The cell voltage of the coin cells was 0.8 V. Therefore, if the negative and positive electrodes contributed equally to the capacitance, their potential ranges would be ±0.4 V from their respective initial potentials—much narrower than the 0.9 V window used in the three-electrode measurements. Within such a restricted potential range, the redox reactions of TMBQ and PBQ did not proceed at the high charge–discharge rate of 5 A g^{-1}, as evidenced by the GCD curves of the asymmetric AC/TMBQ (3)||AC/PBQ (3) cell (Fig. S21d). Nevertheless, unlike at 5 A g^{-1} where the redox reactions did not proceed, the asymmetric AC/TMBQ (3)||AC/PBQ (3) cell at 2 A g^{-1} exhibited a charging time of 73 s. Once this charging time was ensured, the cell delivered a volumetric capacitance 6.3 times greater than that of the symmetric AC||AC cell at 2 A g^{-1}. The gravimetric energy and power densities of the symmetric and asymmetric cells are plotted in Fig. 6c together with those of a symmetric coin cell composed of a commercial EDLC activated carbon (YP-50F), *i.e.*, YP-50F||YP-50F. The corresponding volumetric energy and power densities are presented in Fig. 6d. YP-50F possesses a pore structure dominated by micropores together with mesopores smaller than 3 nm; its micropore and mesopore volumes are 0.66 and 0.10 cm^3 g^{-1}, respectively, with a BET specific surface area of 1520 m^2 g^{-1} (Fig. S22). Because the BET specific surface area of YP-50F is less than half of AC, YP-50F||YP-50F exhibits lower gravimetric energy densities than AC||AC across the entire power-density range. However, because the electrode density of YP-50F (0.504 g cm^{-3}) is higher than that of AC (0.326 g cm^{-3}), the difference in volumetric energy density between AC||AC and YP-50F||YP-50F becomes much smaller. In contrast, except at 5 A g^{-1} (293 W kg^{-1} and 131 W L^{-1}), AC/TMBQ (3)||AC/PBQ (3) exhibits higher gravimetric and volumetric energy densities than AC||AC and YP-50F||YP-50F.

The mean cell voltage (V_{mean}) decreases with increasing current, reflecting resistive voltage losses in the cell (Fig. S23). Here, V_{mean} was calculated as the time-averaged voltage during discharge from immediately after the IR drop to 0 V, and the IR drop (ΔV_{IR}) increased approximately linearly with current (ΔV = IR), yielding internal resistances of 3.45 Ω for the symmetric AC||AC cell and 2.81 Ω for the asymmetric AC/TMBQ (3)||AC/PBQ (3) cell. For comparison, a symmetric YP-50F||YP-50F coin cell exhibited a larger resistance of 7.03 Ω, indicating that the AC-based electrodes provide lower internal resistance than the commercial activated carbon electrode under the present conditions. For the coin-cell measurements (ΔV = 0.8 V), we additionally report capacity-type metrics (mAh cm^{-3}, mAh cm^{-2}, and mAh g^{-1}) converted from the corresponding capacitances *via* $Q = C\Delta V$ (1 mAh = 3.6 C) (Fig. S24). Because QD adsorption occurs within the AC pores without measurable electrode expansion (*vide supra*), and all electrodes were fabricated under identical geometric and processing conditions (see Experimental section), these capacity-type metrics follow essentially the same trends as the corresponding areal/volumetric/gravimetric capacitances.

The cycle test was performed at 2 A g^{-1}, where the asymmetric AC/TMBQ (3)||AC/PBQ (3) cell exhibited a volumetric capacitance that was 6.1 times higher than that of the symmetric AC||AC cell (Fig. 6b). After 10 000 cycles, the symmetric AC||AC and asymmetric AC/TMBQ (3)||AC/PBQ (3) cells retained 102% and 80% of their initial capacitances, respectively. Importantly, despite the gradual fading observed in the asymmetric AC/TMBQ (3)||AC/PBQ (3) cell, its volumetric capacitance remained 4.7 times higher than that of the symmetric AC||AC cell after prolonged cycling. The cycling behaviour of AC/TMBQ (3)||AC/PBQ (3) was found to depend strongly on the electrochemical pretreatment and storage conditions (Fig. S25a). When the cycle test was started immediately after cell assembly, the first-cycle capacitance was extremely small, but increased rapidly during subsequent cycles. In contrast, cells subjected to several CV and/or GCD cycles before the cycling test exhibited much higher initial capacitances and more stable cycling behaviour. A similar tendency was also observed for symmetric AC||AC and YP-50F||YP-50F coin cells, indicating that the low initial capacitance is not specific to the quinone-modified electrodes but is mainly related to electrochemical conditioning of the coin cell with a limited amount of electrolyte (Fig. S25b). Additional analyses of the electrodes recovered from stored or cycled coin cells revealed partial redistribution of TMBQ and PBQ between the negative and positive electrodes (Fig. S26 and S27). These observations indicate that partial desorption and redistribution of quinone species occur during storage and cycling, which likely contribute to the moderate capacitance decrease observed during long-term cycling. Even during prolonged measurements in the coin cells, the characteristic redox potentials of the QDs remained unchanged, indicating that the molecular structures of the QDs are preserved despite partial desorption and re-adsorption of the molecules between the electrodes during long-term operation.

Leakage current and self-discharge are important parameters for evaluating the practical performance and energy retention of electrochemical capacitors.[58] The cells were first charged to 0.8 V at 1 A g^{-1}, after which the leakage current was monitored for 2 h at constant voltage, followed by measurement of the open-circuit voltage for 24 h. The leakage currents after 2 h were 0.046 mA for AC/TMBQ (3)||AC/PBQ (3), 0.047 mA for AC||AC, and 0.037 mA for YP-50F||YP-50F (Fig. 6f), indicating that the incorporation of the QDs does not significantly increase the steady-state leakage current compared with the symmetric AC cell. The self-discharge measurements show that AC||AC exhibits the slowest voltage decay, whereas YP-50F||YP-50F shows the most pronounced voltage drop, with AC/TMBQ (3)||AC/PBQ (3) displaying intermediate behaviour (Fig. 6g). This trend suggests that the porous structure of AC effectively suppresses voltage loss, while the presence of redox-active quinone species slightly accelerates self-discharge compared with AC||AC.

The scalability of the present solvent-free hybridization strategy was examined by a tenfold batch-scale increase, which preserved both the adsorption behaviour and electrochemical performance (Fig. S28). The simplicity of the direct mixing process, which requires neither solvents nor thermal or vacuum treatment, suggests that further scale-up is primarily governed by powder mixing and contact efficiency rather than by intrinsic kinetic limitations. Continuous processing could therefore be

envisaged using established solid-handling technologies, although optimization of residence time and mixing uniformity would be required.

Overall, the results demonstrate that QDs can be effectively hybridized with AC through simple room-temperature adsorption without compromising the pore structure or electrochemical accessibility of the carbon framework. The AC/QD hybrids exhibit enhanced charge storage originating from reversible redox reactions of QDs while maintaining efficient ion transport within the porous electrode. Consequently, the asymmetric AC/TMBQ (3)||AC/PBQ (3) coin cell delivers substantially higher gravimetric and volumetric energy densities than conventional symmetric AC cells while retaining comparable leakage current and acceptable self-discharge behaviour. These findings highlight that solvent-free adsorption of QDs onto porous carbon provides a practical strategy for improving the energy density of aqueous electrochemical capacitors.

Conclusions

In this study, we demonstrated a solvent-free, room-temperature method for hybridizing QDs with AC through direct mixing, thereby eliminating drying, heating, vacuum, and solvent operations. Structural and calorimetric analyses revealed that adsorption is driven by π–π interactions at the AC pore interfaces, and that direct molecular contact is indispensable for hybridization *via* interfacial adsorption at 25 °C. The resulting AC/QD hybrids exhibited distinct redox activity without compromising the porous structure of AC. Electrochemical evaluations showed that the hybrids delivered high volumetric capacitances and improved rate performance, attributable to the interfacial redox reactions of QDs confined within AC pores. In the asymmetric coin cell using AC/TMBQ (3) and AC/PBQ (3) as the negative and positive electrodes, respectively, their narrow potential windows limited redox activity at the very high current density of 5 A g^{-1}, yet at 2 A g^{-1} the cell achieved a volumetric capacitance up to 6.3-fold greater than that of the symmetric AC||AC cell. Compared with symmetric AC||AC and commercial YP-50F||YP-50F cells, the AC/TMBQ (3)||AC/PBQ (3) cell exhibits substantially higher gravimetric and volumetric energy densities while maintaining comparable power capability. In addition, the hybrid cell shows moderate self-discharge behaviour comparable to conventional AC-based cells, indicating that the introduction of QDs enhances energy storage without significantly compromising practical operating characteristics. Furthermore, even after 10 000 cycles at 2 A g^{-1}, the asymmetric AC/TMBQ (3)||AC/PBQ (3) cell retained 80% of its initial capacitance, maintaining a volumetric capacitance that was 4.7 times higher than the symmetric AC||AC cell. These findings highlight the critical role of interfacial adsorption in determining electrochemical behaviour and establish solvent-free room-temperature hybridization as a simple, energy-efficient, and sustainable strategy for preparing durable, high-performance electrodes for energy storage.

Author contributions

Hiroyuki Itoi: conceptualization, data curation, formal analysis, investigation, methodology, project administration, supervision, visualization, writing – original draft; Ryoma Ito: data curation, investigation, validation, visualization; Manato Matsuo: data curation, investigation, validation, visualization; Yusuke Higashi: investigation, validation; Hayato Suzuki: investigation; Ginga Saeki: investigation, validation; Takafumi Ishii: data curation, investigation; Yoshimi Ohzawa: writing – review & editing.

Conflicts of interest

There are no conflicts to declare.

Data availability

The data supporting this article have been included as part of the supplementary information (SI).

Supplementary information is available. See DOI: https://doi.org/10.1039/d5lf00343a.

References

1 Y. Song, J. Phipps, C. Zhu and S. Ma, *Angew. Chem., Int. Ed.*, 2023, **62**, e202216724.
2 J. Wei, X. Zhao, X. Yang, S. Gao, Y. Ji, Q. Lv and X. Wei, *J. Energy Storage*, 2022, **55**, 105840.
3 K. Yanagi, Y. Miyata and H. Kataura, *Adv. Mater.*, 2006, **18**, 437–441.
4 K. Nueangnoraj, H. Nishihara, T. Ishii, N. Yamamoto, H. Itoi, R. Berenguer, R. Ruiz-Rosas, D. Cazorla-Amorós, E. Morallón, M. Ito and T. Kyotani, *Energy Storage Mater.*, 2015, **1**, 35–41.
5 E. J. Son, J. H. Kim, K. Kim and C. B. Park, *J. Mater. Chem. A*, 2016, **4**, 11179–11202.
6 C. Han, H. Li, R. Shi, T. Zhang, J. Tong, J. Li and B. Li, *J. Mater. Chem. A*, 2019, **7**, 23378–23415.
7 T. Uemura, D. Hiramatsu, Y. Kubota, M. Takata and S. Kitagawa, *Angew. Chem., Int. Ed.*, 2007, **46**, 4987–4990.
8 T. Tomai, S. Mitani, D. Komatsu, Y. Kawaguchi and I. Honma, *Sci. Rep.*, 2014, **4**, 3591.
9 C.-F. Chang, C.-Y. Chang and W. Höll, *Ind. Eng. Chem. Res.*, 2003, **42**, 6904–6910.
10 K. Nakasone, S. Kitajima, H. Kasai, K. Oka and D. Takimoto, *ACS Appl. Mater. Interfaces*, 2025, **17**, 44631–44638.
11 S. Isikli and R. Díaz, *J. Power Sources*, 2012, **206**, 53–58.
12 C. Li, Y. Ishii, S. Inayama and S. Kawasaki, *Nanotechnology*, 2017, **28**, 355401.
13 M. Endo, T. Hayashi, H. Muramatsu, Y.-A. Kim, H. Terrones, M. Terrones and M. S. Dresselhaus, *Nano Lett.*, 2004, **4**, 1451–1454.
14 T. Fujimori, A. Morelos-Gómez, Z. Zhu, H. Muramatsu, R. Futamura, K. Urita, M. Terrones, T. Hayashi, M. Endo, S. Young Hong, Y. Chul Choi, D. Tománek and K. Kaneko, *Nat. Commun.*, 2013, **4**, 2162.

15 H. Itoi, Y. Yasue, K. Suda, S. Katoh, H. Hasegawa, S. Hayashi, M. Mitsuoka, H. Iwata and Y. Ohzawa, *ACS Sustainable Chem. Eng.*, 2017, **5**, 556–562.
16 H. Itoi, H. Hasegawa, H. Iwata and Y. Ohzawa, *Sustainable Energy Fuels*, 2018, **2**, 558–565.
17 H. Itoi, S. Tazawa, H. Hasegawa, Y. Tanabe, H. Iwata and Y. Ohzawa, *RSC Adv.*, 2019, **9**, 27602–27614.
18 H. Itoi, S. Kotani, Y. Tanabe, Y. Kasai, R. Suzuki, M. Miyaji, H. Iwata and Y. Ohzawa, *Electrochim. Acta*, 2020, **362**, 137119.
19 H. Itoi, M. Matsuura, Y. Tanabe, S. Kondo, T. Usami and Y. Ohzawa, *RSC Adv.*, 2023, **13**, 2587–2599.
20 H. Itoi, M. Matsuura, T. Usami, Y. Nagai, H. Iwata and Y. Ohzawa, *Carbon Reports*, 2023, **2**, 155–167.
21 H. Itoi, T. Nakamura, S. Tazawa, Y. Nagai, H. Suzuki, R. Ito, G. Saeki, S. Takagi, H. Iwata and Y. Ohzawa, *Carbon Reports*, 2025, **4**, 95–108.
22 H. Itoi, Y. Kasai, H. Hasegawa, K. Yamamoto, H. Iwata and Y. Ohzawa, *Chem. Phys. Lett.*, 2020, **755**, 137795.
23 H. Itoi, T. Ninomiya, H. Hasegawa, S. Maki, A. Sakakibara, R. Suzuki, Y. Kasai, H. Iwata, D. Matsumura, M. Ohwada, H. Nishihara and Y. Ohzawa, *J. Phys. Chem. C*, 2020, **124**, 15205–15215.
24 H. Itoi, Y. Kasai, Y. Tanabe, R. Suzuki, M. Miyaji and Y. Ohzawa, *J. Solid State Chem.*, 2021, **299**, 122149.
25 W. Yu, Z. Shen, T. Yoshii, S. Iwamura, M. Ono, S. Matsuda, M. Aoki, T. Kondo, S. R. Mukai, S. Nakanishi and H. Nishihara, *Adv. Energy Mater.*, 2024, **14**, 2303055.
26 H. Itoi, K. Takagi, T. Usami, Y. Nagai, H. Suzuki, C. Matsuoka, H. Iwata and Y. Ohzawa, *ACS Appl. Nano Mater.*, 2023, **6**, 11541–11552.
27 H. Itoi, S. Maki, T. Ninomiya, H. Hasegawa, H. Matsufusa, S. Hayashi, H. Iwata and Y. Ohzawa, *Nanoscale*, 2018, **10**, 9760–9772.
28 C. Guo, K. Zhang, Q. Zhao, L. Pei and J. Chen, *Chem. Commun.*, 2015, **51**, 10244–10247.
29 K. Nueangnoraj, T. Tomai, H. Nishihara, T. Kyotani and I. Honma, *Carbon*, 2016, **107**, 831–836.
30 G. Muedas-Taipe, M. Badawi, A. M. Baena-Moncada and M. Ponce-Vargas, *Phys. Chem. Chem. Phys.*, 2025, **27**, 12211–12219.
31 A. Rochefort and J. D. Wuest, *Langmuir*, 2009, **25**, 210–215.
32 Ø. Borck and E. Schröder, *Surf. Sci.*, 2017, **664**, 162–167.
33 E. R. Azhagiya Singam, Y. Zhang, G. Magnin, I. Miranda-Carvajal, L. Coates, R. Thakkar, H. Poblete and J. Comer, *J. Chem. Theory Comput.*, 2019, **15**, 1302–1316.
34 X. Chen, H. Wang, H. Yi, X. Wang, X. Yan and Z. Guo, *J. Phys. Chem. C*, 2014, **118**, 8262–8270.
35 S. Li, A. N. Aphale, I. G. Macwan, P. K. Patra, W. G. Gonzalez, J. Miksovska and R. M. Leblanc, *ACS Appl. Mater. Interfaces*, 2012, **4**, 7069–7075.
36 P.-J. J. Huang, R. Pautler, J. Shanmugaraj, G. Labbé and J. Liu, *ACS Appl. Mater. Interfaces*, 2015, **7**, 9898–9903.
37 F. Yan, S. Kumar, K. Spyrou, A. Syari'ati, O. De Luca, E. Thomou, E. M. Alfonsín, D. Gournis and P. Rudolf, *ACS ES&T Water*, 2021, **1**, 157–166.
38 F. Wang, X. Lu, W. Peng, Y. Deng, T. Zhang, Y. Hu and X.-y. Li, *ACS Omega*, 2017, **2**, 5378–5384.
39 G. Sheng, Y. Shao, W. Ye, C. Sun, C. Chen, J. C. Crittenden and C. Liu, *ACS Sustainable Chem. Eng.*, 2018, **6**, 6711–6717.
40 T. R. B. Ramakrishna, M. Mathesh, Z. Liu, C. Zhang, A. Du, J. Liu, C. J. Barrow, M. Chen, M. J. Biggs and W. Yang, *Langmuir*, 2020, **36**, 13575–13582.
41 T. Ishii, *Carbon Reports*, 2023, **2**, 78–90.
42 T. Ishii and J.-i. Ozaki, *Carbon*, 2022, **196**, 1054–1062.
43 G. e. Yuan, G. Zhang, J. Chen, L. Fu, L. Xu and F. Yang, *J. Solid State Electrochem.*, 2013, **17**, 2711–2719.
44 N. An, F. Zhang, Z. Hu, Z. Li, L. Li, Y. Yang, B. Guo and Z. Lei, *RSC Adv.*, 2015, **5**, 23942–23951.
45 Z. Pei, L. Li, L. Sun, S. Zhang, X.-q. Shan, S. Yang and B. Wen, *Carbon*, 2013, **51**, 156–163.
46 M. R. Tuttle, S. T. Davis and S. Zhang, *ACS Energy Lett.*, 2021, **6**, 643–649.
47 H. Itoi, K. Takagi, T. Usami, Y. Nagai, H. Suzuki, C. Matsuoka, H. Iwata and Y. Ohzawa, *Langmuir*, 2024, **40**, 10695–10704.
48 H. Itoi, K. Takagi, H. Ohmi, T. Usami, Y. Nagai, C. Matsuoka, R. Suzuki, S. Kugimiya, H. Iwata and Y. Ohzawa, *ACS Omega*, 2022, **7**, 35245–35255.
49 A. R. Thiruppathi, J. van der Zalm, C.-K. Hung and A. Chen, *ACS Appl. Energy Mater.*, 2023, **6**, 5486–5497.
50 Z. Zhang, L. Wang, J. Xiao, F. Xiao and S. Wang, *ACS Appl. Mater. Interfaces*, 2015, **7**, 17963–17968.
51 L. Xiao, D. Wu, S. Han, Y. Huang, S. Li, M. He, F. Zhang and X. Feng, *ACS Appl. Mater. Interfaces*, 2013, **5**, 3764–3769.
52 Y. Wang, Z. Shi, Y. Huang, Y. Ma, C. Wang, M. Chen and Y. Chen, *J. Phys. Chem. C*, 2009, **113**, 13103–13107.
53 B. Zhang, Y. Wang, K. Cao, Y. Zhang, Y. Xie, C. Liu and Q. Wang, *Energy Fuels*, 2023, **37**, 15637–15646.
54 T. Liu, Z. Zhou, Y. Guo, D. Guo and G. Liu, *Nat. Commun.*, 2019, **10**, 675.
55 T. Li, R. Ma, X. Xu, S. Sun and J. Lin, *Microporous Mesoporous Mater.*, 2021, **324**, 111277.
56 H. Itoi, H. Nishihara, T. Ishii, K. Nueangnoraj, R. Berenguer-Betrián and T. Kyotani, *Bull. Chem. Soc. Jpn.*, 2014, **87**, 250–257.
57 D. Tanaka, N. Takemori, Y. Iba, K. Suyama, S. Shimizu, T. Yoshii, H. Nishihara, Y. Kamimura, Y. Kubota and S. Inagaki, *Microporous Mesoporous Mater.*, 2024, **379**, 113294.
58 W. Shang, W. Yu, X. Xiao, Y. Ma, Y. He, Z. Zhao and P. Tan, *Adv. Powder Mater.*, 2023, **2**, 100075.